Journal of
Micro/Nanolithography,
MEMS, and MOEMS

Nanolithography.SPIEDigitalLibrary.org

Modeling and measuring the transport and scattering of energetic debris in an extreme ultraviolet plasma source

John R. Sporre
Daniel T. Elg
Kishor K. Kalathiparambil
David N. Ruzic

SPIE.

Modeling and measuring the transport and scattering of energetic debris in an extreme ultraviolet plasma source

John R. Sporre,[†] Daniel T. Elg, Kishor K. Kalathiparambil, and David N. Ruzic[*]
University of Illinois at Urbana-Champaign, Center for Plasma-Material Interactions, Department of Nuclear, Plasma, and Radiological Engineering, 216 Talbot Laboratory MC-234, 104 South Wright Street, Urbana, Illinois 61801, United States

Abstract. A theoretical model for describing the propagation and scattering of energetic species in an extreme ultraviolet (EUV) light lithography source is presented. An EUV light emitting XTREME XTS 13-35 Z-pinch plasma source is modeled with a focus on the effect of chamber pressure and buffer gas mass on energetic ion and neutral debris transport. The interactions of the energetic debris species, which is generated by the EUV light emitting plasma, with the buffer gas and chamber walls are considered as scattering events in the model, and the trajectories of the individual atomic species involved are traced using a Monte Carlo algorithm. This study aims to establish the means by which debris is transported to the intermediate focus with the intent to verify the various mitigation techniques currently employed to increase EUV lithography efficiency. The modeling is compared with an experimental investigation. [DOI: 10.1117/1.JMM.15.1.013503]

Keywords: extreme ultraviolet; intermediate focus; debris mitigation; Monte Carlo; elastic scattering.

Paper 15179 received Nov. 10, 2015; accepted for publication Jan. 14, 2016; published online Feb. 5, 2016.

1 Introduction

The contamination and damage of reflective optics, by energetic plasma debris, is a critical issue in extreme ultraviolet light (EUV) lithography tools. EUV lithography sources utilize 13.5-nm light, which is aimed to achieve resolution limits superior to currently utilized 193 nm immersion lithography techniques while also attempting to improve on throughput costs. EUV light emitting plasma can be formed by focusing laser radiation, with a power range of $\sim 10\ \mathrm{W/cm^2}$, onto a mass-limited Sn droplet on the order of tens of microns in diameter.[1] The photon radiation pressure accelerates electrons from the droplet surface into the bulk creating the EUV light emitting plasma through heat and compression. The expanding plasma generates radiation in several wavelengths, including the required EUV light. One key component in the lithography tool is the EUV focusing optics. Since EUV radiation is absorbed into nearly all substances, reflective optics are mandatory. Collector optics may be either multilayer normal incidence mirrors or grazing-incidence reflectors, while downstream mirrors in the optical chain are typically multilayer normal incidence mirrors. Both configurations require highly precise coatings deposited on optically flat base materials. For example, normal incidence EUV reflectors have alternating bilayers of high and low Z, with layer thicknesses determined by Bragg diffraction. One typical configuration is a bilayer of 4.5 nm Si and 2.4 nm Mo. The resulting segment length of 6.9 nm is nearly half the wavelength of the 13.5 nm light, and consequently optimizes Bragg diffraction.[2–4] Such is the precision kept in the multilayer mirrors that either the addition of layers by debris deposition, or the sputtering induced removal of the deposited multilayers, can change the surface properties of the layers and severely disrupt the efficiency and performance of the EUV source.

Generating EUV light requires a considerable amount of energy to excite the Sn atoms into the required highly ionized states (8+ to 12+).[5] The energy requirement is worsened by the fact that less than 6% of total energy input is actually converted into useable EUV light. In addition to heat and out-of-band radiation, such an energetic plasma ($T_e \sim 30$ eV, $n_e \sim 10^{20}\ \mathrm{cm^{-3}}$) generates energetic ions and neutrals, which interact with the buffer gas and wall materials.[6–8] Buffer gas species, through scattering events, can consequently acquire energies significantly higher than the sputtering threshold of the chamber wall materials,[9] or multilayer mirror materials, resulting in sputtering and creation of further debris or erosion of the EUV reflectors. In terms of the redeposition of materials, a typical discharge produced plasma EUV emitting light source can deposit Sn at a rate of 3.2×10^{-8} nm/pulse even with a buffer gas and foil trap in place.[10] This is very detrimental to source operation. For example, considering that manufacturing tools need to run upward of 20 kHz, it would take only hours of operation to deposit 5 nm of Sn on the surface of the collector, which would result in a 70% reduction in the EUV light. However, while much research has been carried out on mitigating debris transport to the collector and on cleaning Sn deposition from the collector,[6,11,12] the collector is not the only mirror in the optical chain. Photons from the collector are focused to the intermediate focus (IF), beyond which the rest of the optical chain lies. Focus must also be placed on understanding the debris transport mechanisms from the plasma source to the IF location, where only the clean EUV photons are allowed to be transmitted.[13]

A theoretical understanding of the observed effects is necessary for implementing various mitigation techniques as well as for anticipating unaccounted for problems. In this

*Address all correspondence to: David N. Ruzic, E-mail: druzic@illinois.edu

†Present address: IBM Corporation, 257 County Road 156, Albany, New York 12203, United States.

1932-5150/2016/$25.00

paper, the creation and transport of energetic debris with a Z-pinch EUV light source is analyzed using the Monte Carlo method and compared to experiment. The developed model operates by creating a test atom, giving it an initial trajectory and energy, and subjecting it to gas scattering and wall-scattering collisions. The model is implemented using MATLAB code, and the effect of chamber pressure and the buffer gas species, on the created energetic species emanating from the EUV plasma is investigated. The results are illustrated using realistic particle trajectory plots. The operating conditions in which the energetic debris reaches the optic conditions are identified. It will be shown that the buffer gas mass and pressure must be chosen in a manner that not only prevents Sn from reaching the IF but also minimizes transport of high-energy buffer gas ions to the IF.

2 Theoretical Model

2.1 *Experimental Setup and Model Domain*

The experimental setup being modeled is the XTS 13-35 EUV light source, which utilizes a pulsed Z-pinch discharge to compress a pre-ionized gas to generate the EUV light. Details describing the technical specifications and the operating range of parameters of the experimental setup are provided in Refs. 7 and 14. In the associated experiments performed, the cathode used is solid Sn, which is ablated by N_2 gas, and introduced into the pinch plasma. The capacitor bank is discharged (2.5 kV, 20 kA, 1 μs) to generate the EUV light emitting plasma (10^{20} cm^{-3}, 30 eV) from the ablated Sn atoms. After the capacitor discharge pulse, the cylindrical pinch plasma expands radially from the source, and the EUV light is emitted along with the out-of-band radiation as well as energetic ions and neutrals, which expands into the chamber. The model takes into account the three-dimensional (3-D) geometry of the chamber, with the chamber wall treated as a perfect cylinder of diameter 0.92 m. To simulate a collector optic, a mock grazing-incidence collector optic was created, consisting of two stainless steel shells. The outer shell was 0.44 m in diameter and designed to reflect 30 deg light while the inner shell was 0.13 m in diameter and designed to reflect 10 deg light. These shells serve to simulate the reflection and transport of energetic debris emanating from the EUV emitting plasma through a grazing-incidence collector, even though they are unable to reflect EUV light. The brackets that support the shape of the shells obscured direct line of sight from the EUV plasma source to the IF similar to those used in industry. The model geometry is shown in Fig. 1, and the exact dimensions used are provided in Table 1. Cartesian coordinates were used.

Experimental diagnostics were performed by the Sn intermediate focus flux emission detector (SNIFFED). At the IF is a differential pumping gasket with a 1-mm radius. SNIFFED is located beyond this gasket and contains multiple diagnostics placed on a ring positioned to intersect the 10 deg specular reflection. In the model, the gasket orifice was given a radius of 10 cm to allow for the capture of enough computational atoms; this discrepancy between model and experiment was later remedied as part of a calibration factor, detailed in Sec. 5. The most relevant diagnostic for this work is a set of microchannel plates (MCPs), which measure the flux of energetic ions and neutrals to the IF. The fluxes measured by these plates were compared with those calculated by the model. Additionally, Si witness plates were used to measure solid debris deposition. Since this included C (from pump oil) and Cu (from the anode), x-ray photoelectron spectroscopy (XPS) was used to quantify how much of the deposition consisted of Sn debris. Full detail of the SNIFFED apparatus is provided in Ref. 13.

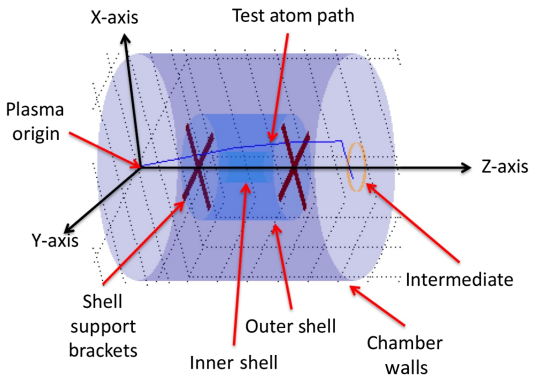

Fig. 1 Chamber geometry considered in the model, which resembles the actual experimental chamber in dimensions. It consists of the two shells included to act as a mock-up collector optic, the brackets that support these shells and block direct line of sight between the plasma and the IF. The modeled size of the IF is much larger compared to the actual size.

Table 1 The dimensions of the modeled chamber and the mock-up collector optic components (denoted as inner and outer shells in Fig. 1).

Shell name	Radius (m)	Length (m)	Distance from plasma (m)
Inner shell	0.064	0.15	0.285
Outer shell	0.216	0.305	0.2075
Chamber walls	0.46	0.72	0.0
IF	0.1	0.0	0.72

2.2 *Creation of a Test Atom*

At the beginning of each computational trial, a test atom is created with an initial energy and trajectory, and then undergoes gas-scattering or wall-scattering collision events until it reaches a required threshold for elimination. The assigned values of the initial energy were based on the experimentally obtained values from the energy analysis of ions and neutrals using a spherical sector electrostatic energy analyzer.[15,16]

The total flux measured at the detector for an N_2 fueled pinch is shown in Fig. 2. Such a curve was utilized for determining the initial energy of the test atom. For the model, the total flux curve was normalized to determine the probability of an atom being at a given energy. A random number generator was used to select energies between 0 and 50 keV according to probabilities given by the measured spectrum.

Similarly, the initial direction vector of the test atom was assigned using a cosine distribution probability function [Eq. (1)], which adhered to experimental angular measurements

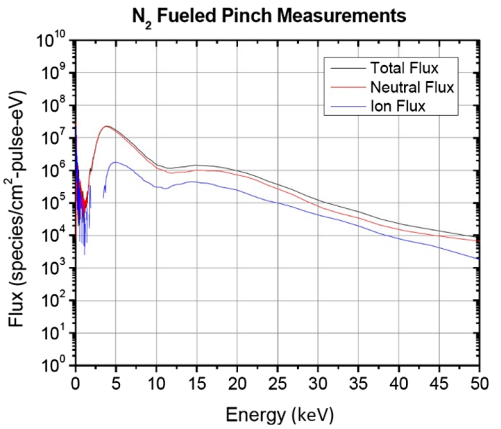

Fig. 2 The total and neutral flux measured by the detector during the pinch operation with N_2 as the fuel gas. The ion flux is therefore obtained from the difference.

$$f(x,\mu,\mathrm{s}) = \frac{1}{2s}\left[1 + \mathrm{Cos}\left(\frac{x-\mu}{s}\pi\right)\right]. \quad (1)$$

In this equation, f is the probability distribution function, μ is the centroid of the cosine distribution, $\mu + s$ is the rightward boundary of the function, and $\mu - \mathrm{s}$ is the leftward boundary.[17] The assumption of azimuthal symmetry allows for a random value from 0 to 2π to be chosen for θ also. The angular values thus obtained in spherical coordinates are then converted to Cartesian coordinate-based vectors. The chosen randomization resulted in the desired cosine distribution to mimic the angular spectra from the cylindrical Z-pinch plasma.

2.3 *Collisions*

The flow chart shown in Fig. 3 outlines the various collision schemes followed in the model and defines the resulting new generations of test atoms as the test particle is released into the system.

The model starts by running a loop that determines the test atom's new location if no collisions occur. Initially, a timestep of 10^{-6} s is assigned. The projected (collisionless) distance is determined by Eq. (2)

$$\bar{r}_p - \bar{r}_i = \bar{v_p}t. \quad (2)$$

In this Eq. (2), r_i is the initial location vector, r_p is the projected new location vector, v_p the velocity vector (as derived from the energy and mass of the test atom), and t is the time step.

The model then proceeds to calculate the nearest distance to a surface where wall collision interactions need to proceed. If this distance is shorter than the difference between the initial and projected positions, the outcome of a potential wall collision is determined. The code then calculates whether or not a gas-atom collision occurred while traversing the shorter of the two distances; if a collision did occur, the new location is noted. In the case of either a wall collision or a gas-atom collision, the new location of the test atom is set at the point of the collision, and the trajectory and energy of the atom is adjusted. The main loop then repeats itself, moving the test atom from collision to collision until an end point is reached. If no collisions occurred during the timestep, the energy and direction remain the same, since any long-distance attractive or repulsive forces are neglected (even at the operating pressures considered) to maintain computational simplicity. The handling of wall-scattering and gas-scattering collisions is discussed in detail, in Secs. 2.3.1 and 2.3.2.

2.3.1 *Wall-scattering collisions*

Wall collisions are handled separately from gas collisions in the model. The first step in determining if a test atom has undergone a collision is determining the point of intersection with the nearest wall surface. Given the default (collisionless) projected location (x_p, y_p, z_p) and the initial location (x_i, y_i, z_i), a 3-D parametric equation is derived as a function of t [Eqs. (3)–(6)]. In these equations, it is important to note that $t = 0$ represents the starting location and $t = 1$ represents the projected location

$$X(t) = (x_p - x_i)t + x_i, \quad (3)$$

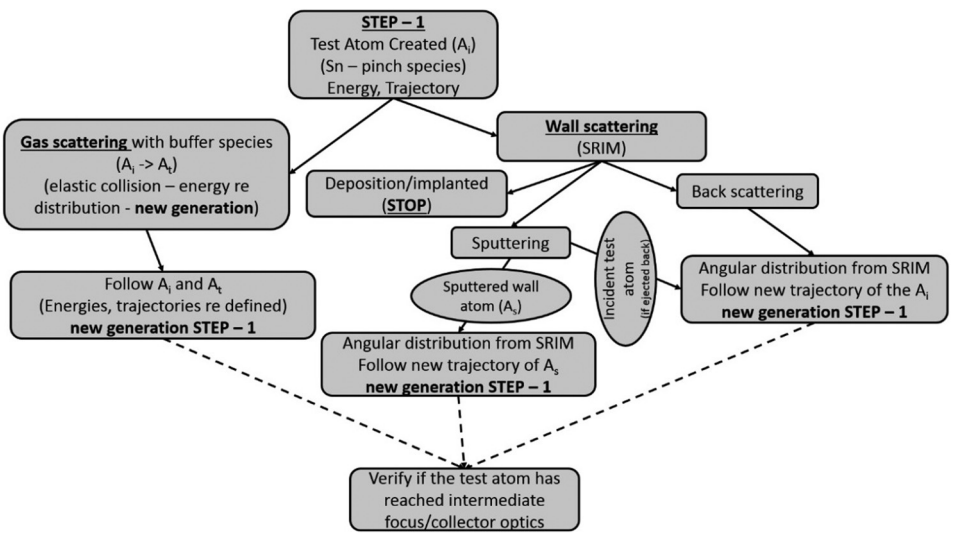

Fig. 3 The flow diagram showing the collision processes of the test atom, as considered in the model.

$$Y(t) = (y_p - y_i)t + x_i, \tag{4}$$

$$Z(t) = (z_p - z_i)t + x_i, \tag{5}$$

$$X(t)^2 + Y(t)^2 = R^2. \tag{6}$$

The wall collision code is then broken into three collision-determining parts: collisions with inner cylinder surfaces, collisions with the near pinch and near IF planar walls, and collisions with the brackets that support the collector optics. The value of t is calculated for each of these surfaces. For collisions with cylinders (inner shell, outer shell, and cylindrical chamber wall), Eq. (6) is solved with R equal to the radius of each cylinder. Negative values of t are discarded; for positive values, it must be determined whether the corresponding value of $Z(t)$ resides with the distances assigned to the shells. Cases that do not meet that requirement are discarded. For the planar chamber walls (where the pinch and IF are located), Eq. (5) is solved with the value of $Z(t)$ set to either 0 (pinch location) or 0.72 (IF-containing wall). Finally, for the support brackets, Eq. (6) is solved with $Z(t)$ set as the distance from the plasma for each set of brackets. The resulting value of t is plugged into Eqs. (4) and (5) to compute values of $X(t)$ and $Y(t)$. If the values of $X(t)$ and $Y(t)$ lie within the brackets' dimensions, the positive value of t is kept; otherwise, it is discarded. From the compiled list of t values, the smallest positive value is selected. If this value is greater than 1 or if there are no positive values, no wall collision occurred. However, if there is a positive value less than 1, then a wall collision did occur (pending the possibility of a gas collision, which will be discussed in Sec. 2.3.2).

Proceeding with the assumption that the test atom was found to participate in a wall collision, and that a gas-atom collision did not occur in the process of reaching the wall, it is now necessary to understand how the incident atom will interact with the surface. In this model, there were two possible consequences of the incident atoms interaction with the surface: deposition and reflection. With each of these possibilities, there also exists the potential for sputtering to occur; this will be addressed later. When an energetic atom impacts a surface, it is possible that the atom will not penetrate the outer surface potential because of insufficient energy, or it could possibly traverse a few monolayers of the surface and backscatter back out of the surface. The description of this process is complicated and very difficult to analytically describe with a single equation, and is certainly not describable by the specular reflection properties enjoyed with photons. For the purposes of the debris transport model, it is very important to be able to simulate this process, so a set of scattering properties were calculated using the stopping and range of ions in matter (SRIM) code developed by Ziegler et al.[18] This SRIM code takes the inputs of ion mass, surface composition, ion energy, and angle of incidence, and calculates how the ion will interact with the surface. SRIM itself is a Monte Carlo simulation that models the reaction of surface atoms to the displacement and momentum transfer caused by an incident atom. An output file is created at the end of the simulation, which contains energy, direction (in Cartesian coordinates), and mass information about each of the atomic species that leaves the surface due to sputtering or back scattering (which will be the incident ion itself). The incident atom is monitored to determine whether it is deposited into the surface or backscattered away from the surface, and its final energy and direction (or location in the surface if it is deposited) are noted as well. The directional cosines of each of the relevant species are provided as well.

SRIM simulations were carried out separately before running the main code. For each incident atom species, a look-up table was created containing the deposition probability, backscattering probability, sputtering probability, ratio of sputtered atoms per incident sputtering ion, average backscattered atom energy, and average sputtered atom. The details of the SRIM calculations are not elaborated here. It was evident from the SRIM analysis, for the energy range relevant to this model, that the ion energy is the only major influence on the sputtering yield and the average energy of the sputtered species. For all other parameters, the predominant determining factor is the angle at which the incident ion collides with the surface being sputtered. Since one single SRIM analysis does not account for all possible atom-surface interactions, 1000 individual runs were performed for each energy and angle condition to average out case by case variations. The surface composition of interaction was constructed as a 5-nm layer of Sn deposited on top of a stainless steel substrate. The Sn layer is included to account for the fact that most of the mock-up collector optic surfaces were covered by more than a few nanometers of Sn (as well as other electrode materials) at the end of each hour-long experiment. Even at only 5 nm, SRIM modeling suggests that almost no stainless steel species are capable of being sputtered out of the Sn surface. This is independently verified by XPS of Si witness plates positioned inside the chamber in an effort to experimentally characterize the various species deposited on different parts of the chamber during experiments.

The SRIM code also provides a way of estimating the backscatter direction of incident atoms that do not deposit on the surface. A backscattered or sputtered atom's new direction can be characterized by two angles. As shown in Fig. 4, a test atom collides with a surface at an angle of incidence θ_{incident}, with respect to the surface normal vector. The backscattered direction can be described as a function of the angles $\theta_{\text{scattered}}$, and θ_{straggle}. While these angles are complexly coupled to intrasurface scattering, they can adequately

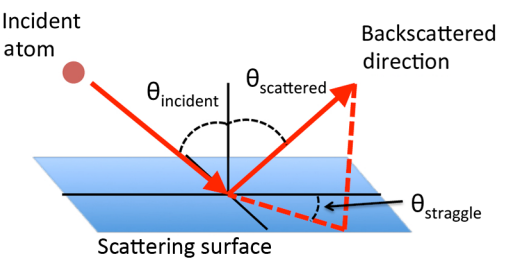

Fig. 4 The relative angles representing the wall-scattering process. For the incident atom, the SRIM code considers the angles relative to the surface normal. A backscattered atom will leave the surface with an angle of $\theta_{\text{scattered}}$ from the surface normal, and an angle of θ_{straggle} away from the plane that is comprised of the incident vector and the surface normal vector. These two angles are able to be approximated using cosine distribution functions.

be described by a cosine distribution fit. Furthermore, the geometry of the problem lends itself readily to the spherical coordinate system. As such, it is simple to convert from the Cartesian vector coordinates provided by SRIM, to the two characterizing angles.

The last part of the wall collision calculations involves determining the backscatter direction vector based on the acquired cosine distributions coefficients for a test atom with known mass, energy, and angle. Because the coefficients are only calculated for a discrete number of conditions, it is first necessary to linearly extrapolate values for a given energy value and angle of incidence. This extrapolation was performed using the three data points closest to the desired energy and angle values. This is performed twice for the scattering and straggling angles to create the new direction vector R for the test atom that has undergone a wall-scattering collisions.

The energy for backscattered atoms is derived from the SRIM-generated look-up table, an adjustment is made to the test atom variable, and a collision is accordingly noted in the test atom's history log. It is important to mention that the same process is used for determining the scattering angles, straggling angles, and resulting energy, of the species that are sputtered out of the surface. The only difference between the two processes is that the scattering angle of the sputtered species is modeled as a random angle from $(0,2\pi)$ because there is no preferred directionality of the species that are sputtered out of the surface layer. The probability of sputtering is determined from the SRIM tables and four-point estimate process, as is the number of sputtered atoms that should be expected per sputter inducing incident ion.

2.3.2 *Gas-scattering collisions*

If no wall collision occurred, there is still a potential for a gas collision as the test atom traverses its mean-free path. Additionally, even if a test atom was projected to collide with a wall, it is still possible for a gas collision to occur first, preventing the atom from reaching the wall. The first step in handling gas-atom collisions is the determination if and where such a collision occurs. Only elastic collisions are considered and the mean-free-path λ is determined by Eq. (7),

$$\lambda = \frac{1}{n\sigma}, \tag{7}$$

where, n is the density of the buffer gas species and σ is the elastic-scattering cross-section. The buffer gas density is determined by the ideal gas law as given by Eq. (8), assuming a temperature of 295 K,

$$P = nRT. \tag{8}$$

The probability of traveling a distance d_0 without undergoing an elastic-scattering collision is then given by P_0 as in Eq. (9),

$$P_0 = \mathrm{e}^{-\frac{d_0}{\lambda}}. \tag{9}$$

The value of d_0 is selected as either the distance the test atom travels before a wall collision, or the distance it would travel in the default time step, whichever distance is shorter. Initially, a random value between 0 and 1 is chosen and compared to the probability of survival. If the random value is larger than the value determined by Eq. (5), a collision is deemed to have occurred. The actual distance traveled before the collision is determined using the cumulative distribution function [Eq. (10)]

$$r_0 = -\lambda \ln(1 - P_x), \tag{10}$$

where P_x is a random value between 0 and the maximum value of the survival probability in the total distance originally tested [given by $(1 - P_x)$].

Classical scattering theory is utilized to determine the collision parameters resulting in a new direction and energy for the incident and scattered species, as shown in Fig. 5.[19]

Energy [Eq. (11)] and angular momentum [Eq. (13)] are conserved in the elastic collision center mass (COM) problem within the coordinate system (r, ϕ)

$$E_{\mathrm{COM}} = V(r) + \frac{1}{2}\mu(r'^2 + r^2\phi'^2); \tag{11}$$

$$\mu = \frac{m_1 m_2}{m_1 + m_2}; \tag{12}$$

$$vb = r^2\phi'. \tag{13}$$

Here, E_{COM} is the total center-of-mass energy of the binary system, $V(r)$ is the interatomic potential between the two atoms, μ is the reduced mass as defined by Eq. (12), b is the impact parameter, and v is the incident atom velocity. The interatomic potential between each species was determined using a combination of the repulsive Abrahamson potential coupled with an attractive well determined based off of the Lennard-Jones potential with a fitting parameter to couple the two different potentials.[20] The fitting parameter is determined roughly by trying to match the slopes of the rise visually. In reality, for the energies being examined in this paper, this ad hoc fitting process adds very little error to the measurement. The resulting potential is described by Eq. (14) and the fitting parameters given in Table 2,

$$V(r) = A\mathrm{e}^{-Br} + 4\varepsilon\left[\left(\frac{\sigma}{r}\right)^x + \left(\frac{\sigma}{r}\right)^6\right]. \tag{14}$$

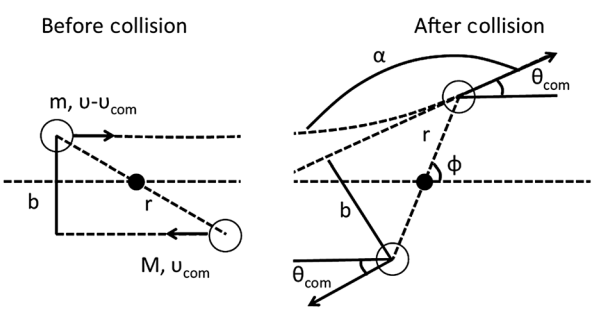

Fig. 5 The COM diagram of the collision between an atom with the mass m and velocity $v - v_{\mathrm{COM}}$ incident on a resting mass M with a (relative) velocity—v_{COM}. The resulting collision has a nearest impact point of r_0 and scattering angle of θ_{COM}. Figure taken from Ref. 19.

Table 2 The six fitting parameters for the Abrahamson type potential with attractive well for use in Eq. (17) to calculate elastic-scattering iterations.

Reaction	ε (eV)	ε (A)	A (eV)	B (eV)	x	Source
Sn–He	0.0191	2.70	2695.16	3.85	6.5	21–23
Sn–Ne	0.0248	2.81	9840.96	3.65	8	21–23
Sn–Ar	0.0465	3.09	14695.64	3.58	7	21–23
Ar–He	0.0031	2.95	1276.62	3.90	6.2	21 and 22
Ar–Ne	0.0058	3.07	4661.38	3.70	6.5	21 and 22
Ar–Ar	0.0108	3.35	6960.90	3.63	6.5	21 and 22
He–He	0.0009	2.56	234.13	4.17	6.1	21 and 22

Equation (14) was plugged into Eq. (11). Equations (11), (12), and (14) were then combined and manipulated according to a process shown in Ref. 19 to calculate the center-of-mass scattering angle, θ_{COM}, as a function of impact parameter, b, and center-of-mass energy, E_{COM}. A grid of b values from 0 to 10 Å with 0.1 Å increments is created, along with a grid of E_{COM} values from 1 to 50,000 eV, with 10 points per decade. The resulting table was used as a look-up-table for gas-scattering collisions to determine θ_{COM}. A sample of θ_{COM} curves (for Sn–Ar collisions) as a function of b for different energies is shown in Fig. 6.

It is evident in the Sn–Ar atom–atom interaction that as energy is increased, the scattering angle is reduced for a given impact parameter. The decrease in interaction potential also results in a reduction of the elastic-scattering cross-section, meaning that at higher energies gas-atom collisions are less likely. For very low energies, ($E > 0.25$ eV, since the lower limit for energy of the species is set to 0.25 eV for computational speed) the scattering angle becomes negative at a finite separation point. In this impact parameter range, a quasibound state forms and the incident species is backscattered.[24]

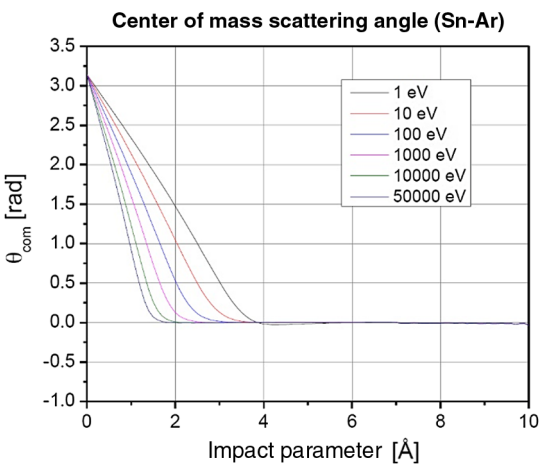

Fig. 6 A representative set of center-of-mass scattering angles is provided for the Sn–Ar collision. As the energy of the incident atom is increased, the maximum impact value (the value at which less than 1% scattering occurs) decreases and very few of the incident atoms are backscattered.

At this point, it was necessary to define the method of choosing the impact parameter. Additionally, the total elastic-scattering cross-section was required in order to calculate the mean-free-path according to Eq. (7). Both the impact parameter and the cross-section can be determined from the maximum impact parameter, b_{max}, which is defined as the distance beyond which θ_{COM} is less than 1 deg. This quantity was determined for the various values of E_{COM} by means of the previously-calculated θ_{COM} look-up-tables, yielding tables of b_{max} as a function of energy for the different collisions. These tables were then easily converted to tables of scattering cross-section as a function of energy by means of Eq. (15),

$$\sigma = \pi b_{max}^2. \tag{15}$$

Additionally, the actual impact parameter to be used in a given collision is related to the maximum impact parameter by Eq. (16),

$$b = \sqrt{P} b_{max}, \tag{16}$$

where P is a random value uniformly distributed between 0 and 1 (inclusive). Since look-up-tables for both b_{max} and σ are defined only at discrete energy values, linear interpolation between the two nearest points is used to calculate b_{max} and σ for the energy in any given collision.

After determining the scattering angle θ_{COM}, the energies and directions of the incident and scattering species in the lab frame can be determined. Using Fig. 7 as a reference, the velocities of each of the individual species can be written as shown in Eqs. (17)–(22)

$$\overline{v_1} = v_1 \hat{x}; \tag{17}$$

$$\bar{v}_2 = -\frac{m}{M} v_2 \hat{x}; \tag{18}$$

$$\bar{v}_1' = v_1 \cos(\theta_{COM})\hat{x} + v_1 \sin(\theta_{COM})\hat{y}; \tag{19}$$

$$\bar{v}_2' = -\frac{m}{M} v_2 \cos(\theta_{COM})\hat{x} - \frac{m}{M} v_2 \sin(\theta_{COM})\hat{y}; \tag{20}$$

$$\bar{V}_1' = \left(1 + \frac{m}{M}\right) v_1 \hat{x}; \tag{21}$$

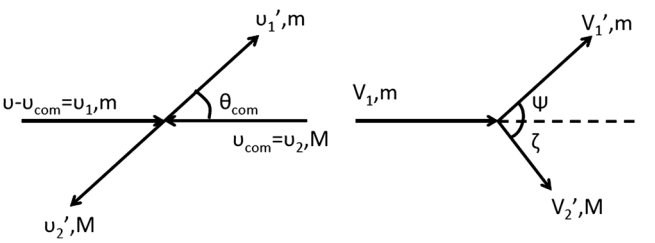

(a) Center of mass frame (b) Lab frame

Fig. 7 In the center-of-mass frame (a), both the incident and the scattering particle travel away from each other at the same angle. In the lab frame (b), individual angles and velocities for each particle need to be determined.

$$\bar{V}_2' = \frac{m}{M}[1 - \cos(\theta_{\mathrm{COM}})]v_1\hat{x} - \sin(\theta_{\mathrm{COM}})v_1\hat{y}. \tag{22}$$

If ε is the total energy of the center-of-mass frame and E the total energy of the lab frame, the energies of each individual species pre- and post-collision can be defined by Eqs. (23) and (24),

$$E = \frac{1}{2}m(V_1)^2 = \frac{1}{2}m(V_1')^2 + \frac{1}{2}M(V_2')^2; \tag{23}$$

$$\varepsilon = \frac{1}{2}m(v_1)^2 + \frac{1}{2}M(v_2)^2 = \frac{1}{2}m(v_1')^2 + \frac{1}{2}M(v_2')^2. \tag{24}$$

Combining the two energy equations reveals the relationship, as shown in Eq. (25), between the lab frame energy and the center-of-mass frame energy, which will always be less than the lab frame energy.

$$E = \left(\frac{m+M}{mM}\right)\varepsilon. \tag{25}$$

Furthermore, it is possible to define the individual energies in terms of the total energies as shown in Eqs. (26)–(29).

$$\varepsilon_1 = \varepsilon_1' = \left(\frac{M}{m+M}\right)\varepsilon; \tag{26}$$

$$\varepsilon_2 = \varepsilon_2' = \left(\frac{m}{m+M}\right)\varepsilon; \tag{27}$$

$$E_1' = \left[\frac{m^2 + 2mM\,\cos(\theta_{\mathrm{COM}}) + M^2}{(m+M)^2}\right]E; \tag{28}$$

$$E_2' = \left\{\frac{2mM[1 - \cos(\theta_{\mathrm{COM}})]}{(m+M)^2}\right\}E. \tag{29}$$

The values of E_1' and E_2' are the postscattering energies of the scattered species (incident and the scattering atoms). These values are needed to determine the exit velocity of the test atom in question, and the newly created scattered species in the debris transport model. The different lab frame scattering angles are deduced by geometry in addition to the equations of path, and are shown in Eqs. (30) and (31).

$$\tan(\psi) = \frac{\sin(\theta_{\mathrm{COM}})}{\cos(\theta_{\mathrm{COM}}) + \frac{m}{M}}; \tag{30}$$

$$\tan(\zeta) = \frac{\sin(\theta_{\mathrm{COM}})}{1 - \cos(\theta_{\mathrm{COM}})}. \tag{31}$$

With the newly directed species' energies and directions determined, the last remaining step in modeling the gas-scattering collisions involves taking the direction from the xy-plane to the plane of reference where the atom is located in the model. The actual collision point between the two species is determined by two parameters. The first is the impact parameter, b. This defines the location along the radius where the collision occurred, providing information on the scattering angle relative to the two species. In order to determine final directions, however, it is necessary to determine the azimuthal location of the point of impact at the given radius b. This is done at random from a value of $(0,2\pi)$. The two calculated vectors of the scattered species are then rotated, in the same manner as the wall-scattering event, until they are in the original 3-D location facing the appropriate direction.

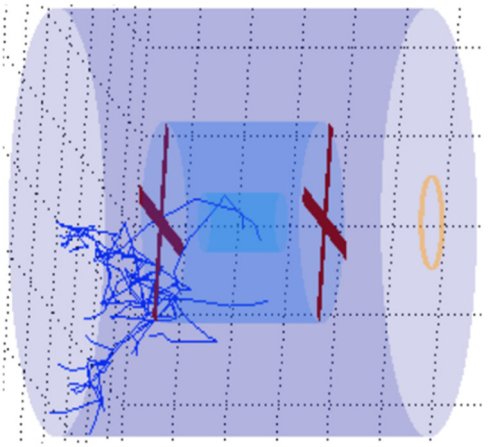

Fig. 8 Shown is a 10 keV Sn atom's path through the 10 mTorr Ar gas environment in the chamber. The fingers that appear are the plots of the secondary generation of scattered Ar atoms. No wall sputtering occurred in this trial.

2.4 *Sample Results*

As a graphical example of the model's capabilities, Fig. 8 shows the trajectory of a 10 keV Sn atom traveling through a 10 mTorr Ar environment and the resulting interactions with the buffer gas atoms. The evolution of the second generation (the scattered species by the first test atom) as the scattered argon species travel through the chamber is shown by the branching trajectories. In this particular example, no energetic atoms reach the IF. However, it is obvious that many scattering events occur, and many Ar atoms are energized by collisions with just one Sn pinch atom.

In order to quantify the number of energetic atoms reaching the IF for various pressures, buffer gas masses, and pinch gas masses, 10,000 Sn atoms were used for each case, and the number and energies of atoms reaching the IF were recorded. Since each pinch atom produces many energetic buffer gas atoms, simulations were limited to the first energetic buffer gas generation in order to perform the simulations in a reasonable amount of time. For this reason and others, it was necessary to calibrate the theoretical IF flux results to the experimental IF flux results. This calibration process will be shown in Sec. 3.

3 Calibration to Experiments

Due to the nature of the experimental diagnostics and computational limitations, a calibration factor must be determined in order to accurately compare the model output to experiments. Rather than measuring direct flux, MCPs measure units of "hits." This hit count is dependent on the energy of the incident flux. Since buffer gas atoms are energized at different energies and at different locations in the chamber, each measured atom travels a different distance. This renders time-of-flight analysis unusable, and the energies of the

measured incident atoms cannot be determined. Therefore, rather than converting the MCP hits into fluxes, the computational fluxes must be converted to a hit value that would be observed if MCPs were to measure the atoms created by the model. This calibration process is detailed here.

First, the species of the measured atoms must be determined. The MCPs have a low-end sensitivity threshold below 100 eV; consequently, any impact by an atom with less than this threshold energy does not produce an electron cascade large enough to measure. Thus, background room temperature gas impingement cannot be measured; however, it is possible to measure the energetic atoms emanating from the EUV-emitting plasma. Two signals are detected. The first, occurring in the first 100 μs, is difficult to precisely measure and is due to the arrival of the scattered high-energy pinch-origin species. The second flux, beginning around 250 μs after pinch formation, is due to the expansion of the energized buffer gas in the chamber. This is known to be the buffer gas because, as shown in Fig. 9, changing the pinch gas mass while leaving the buffer gas constant does not cause a change in the arrival time of this second signal.

Having determined that the main contributor to the hits measured at the IF is energized buffer gas, a calibration may be carried out to convert the number of modeled buffer gas atoms reaching the IF to a modeled number of hits, followed by a comparison of model to experiments.

Two scaling factors caused by the computational setup are readily apparent. First, computational atoms must be converted to real atoms. Due to time constraints, each iteration of the model began with 10,000 test atoms of the pinch gas species, which proceeded to create energetic buffer gas atoms through collisions. Thus, the modeled atoms must be divided by 10,000 and multiplied by the total measured flux of energetic pinch atoms emanating from the pinch. This flux can be measured by placing MCPs on the z-axis in place of SNIFFED without the mock-up collector shells present. An example of this measurement, for N_2, is shown in Fig. 2. Second, though the actual IF had a 1-mm radius, the modeled IF was enlarged to have a 100-mm radius in order to reduce discretization error. Accordingly, the number of atoms reaching the modeled IF must be reduced by a ratio of the actual IF area to the modeled IF area.

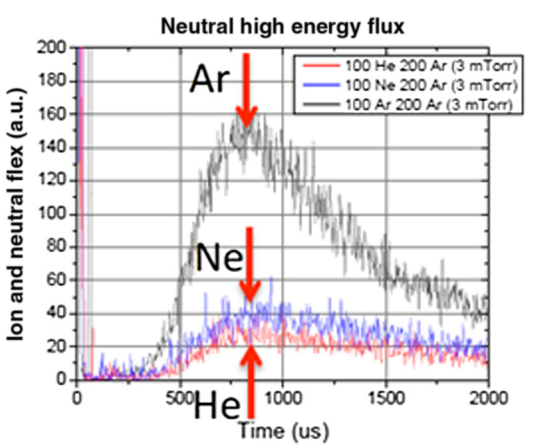

Fig. 9 When the buffer gas is kept as Ar, increasing pinch gas mass from 4 to 40 AMU serves only to increase the amount of energy deposited in the buffer gas species, due to more efficient energy transfer as the pinch gas mass approaches the buffer gas mass. The arrival time of the energetic flux peak, however, is the same for each pinch gas species, suggesting that buffer gas is the key contributor to the flux arriving after 250 μs.

In order to convert modeled atoms to hits that would be observed with real MCPs, scaling factors derived from the nature of MCPs must also be applied. Full information about MCP calibration may be found in Ref. 15. To account for MCP mass sensitivity, the computational atoms are multiplied by the ratio of the buffer gas mass to the mass of Xe, which was the species that was used to experimentally calibrate the MCPs. Additionally, to calculate the number of computational atoms that would be detected by real MCPs, the number of computational atoms must be multiplied by the detector efficiency at the average energy of the incident computational atoms. Next, the resulting number of detected computational atoms may be converted to computational hits by dividing by the base calibration of the MCPs (~204 atoms/hit).

Lastly, errors are still inherent in the computational scheme and the measurement of total flux from the pinch. The experimental measurements of the total flux, shown in Fig. 2, were taken only at a 0 deg angle from the pinch, and the angular distribution of flux was assumed to behave like a cosine distribution; in reality, the extremely energetic species are forward-peaked, and the lower-energy species have a more uniform distribution. Since this measurement was used to convert computational atoms to a corresponding number of real atoms, this induces error in the theoretical results. Additionally, due to computational complexity, only one generation of scattered buffer gas was followed in the model. This causes an underestimation in the theoretical predictions. Finally, the model used Sn pinch atoms. However, it was unknown how much of the original flux emanating from the pinch was due to Sn and how much was due to the pinch feed gas.

A final calibration factor must be applied to the theoretical predictions to account for these errors. This factor was determined by dividing the experimental hit count by the computational hit count and taking an average of this quotient over the course of 10 experiments. This factor amounted to ~158. Once this one calibration factor was obtained, it was used uniformly in the calibration of model data for all experiments.

4 Experimental Results

To compare experiment to model and to analyze the processes by which debris is transported to the IF, experiments were carried out to isolate variations in energetic debris transport due to chamber pressure, buffer gas mass, and pinch gas mass.

4.1 *Pressure*

The pressure was varied from 0.3 to 22 mTorr with Ar as the buffer gas and N_2 as the pinch gas. The flow of N_2 was kept constant at 100 sccm. For the higher pressures (6, 12, and 22 mTorr) the Ar flow was 1000 sccm, and pressure was varied by means of a gate valve in front of the pump. For the 2-mTorr case, the flow of Ar was 200 sccm. For the 0.3-mTorr case, the flow of Ar was set to 0; however, a small amount of Ar was still present in the chamber due to pumping down from a higher pressure. Results shown in Fig. 10(a) agree well with the model

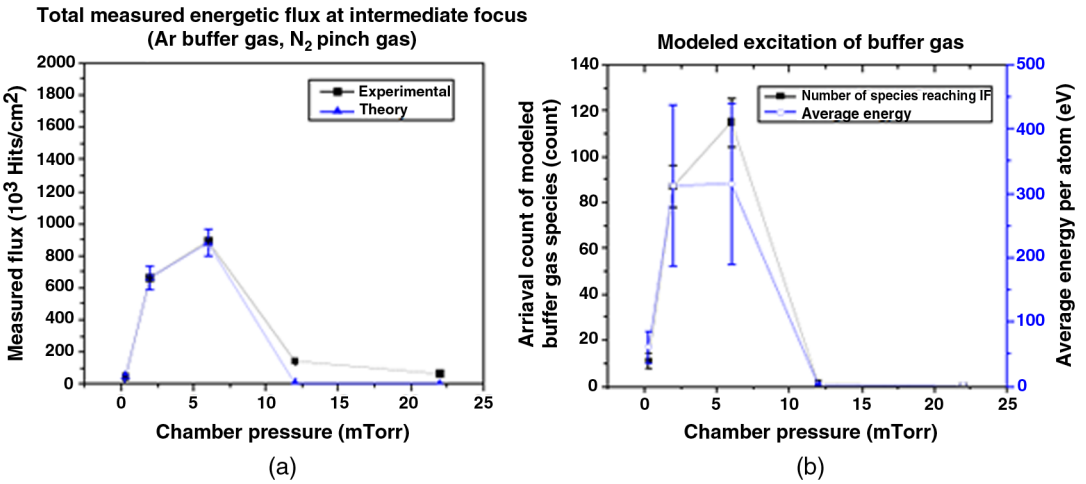

Fig. 10 (a) The theoretical and experimental measurements of energetic flux at the IF are in good agreement as the pressure is varied from 0.3 to 22 mTorr with Ar buffer gas. At 2 and 6 mTorr, Sn collides with Ar and transfers energy, sending energetic Ar through the IF. At 12 and 22 mTorr, the low mean-free-path inhibits the transport of energetic buffer gas to the IF. (b) The trends concerning the two different components of energetic flux (energy and number of atoms) are shown. At high pressures, the energies and numbers of Ar atoms at the IF are low. At 2 and 6 mTorr, however, the energies and numbers are both high.

predictions. Additionally, as shown in Fig. 10(b), the model can be used to analyze not just the flux but the number of species arriving at the IF, as well as their incident energies. This ability lends insights that the MCPs cannot provide.

As shown in Fig. 10(a), there is an intermediate pressure (6 mTorr) at which the flux of energized buffer gas to the IF is maximized. At 0.3 mTorr, few buffer gas atoms are present. Additionally, the large mean-free-path causes wall collisions to be dominant and allows most energized buffer gas to collide with walls and deposit their energy there, rather than scattering off of other atoms and reaching the IF. As shown in Fig. 10(b), collisionality at 2 and 6 mTorr causes both increased energy deposition in the buffer gas and increased scattering of buffer gas atoms, allowing them to reach the IF before colliding with a wall. However, at higher pressures, the mean-free-path becomes small enough that most energized Ar atoms lose their energy through gas collisions and are blocked from the IF. The error in the model-theory comparison in Fig. 10(a) at 12 mTorr is due to discretization error in the model; only one computational atom reached the IF.

Sn deposition results are shown in Fig. 11.

Both theoretical and experimental results show the same trends: the Sn deposition at the IF is maximized at 2 mTorr, decreasing as the pressure increases to higher levels. Good suppression (no Sn deposition) is observed at 12 and 22 mTorr. At 2 mTorr, buffer gas collisions scatter Sn debris away from walls and toward the IF, but there are not enough collisions to thermalize and block the Sn debris from the IF. At 6 mTorr and above, the model agrees with experiments; however, at the two lowest pressures, the model underestimates the Sn deposition. This is because the model assumes that all Sn is coming from the pinch. However, the phenomena of electrode arcing and sputtering can introduce low-energy Sn that is not energized by the pinch and, consequently, was of too low energy to be detected by the MCPs used to calibrate the model and produce the modeled pinch atom energy distribution. Arcing is caused by spatially nonuniform currents at low pressures. When arcing occurs, a pinch is not created, and micron-sized particles are ejected from the "hot spot" on the Sn electrode. At low pressures, these particles can make their way to the IF. Additionally, even when the system pinches and does not arc, Sn is sputtered from the electrode by the plasma; indeed, it is this process that introduces Sn into the pinch. However, some sputtered Sn does not make it into the pinch and instead is simply released into the chamber with the low energies typical of sputtered atoms. At high pressures, these undetected low-energy atoms are easily stopped by buffer gas; at low pressures, however, they can make their way to the IF.

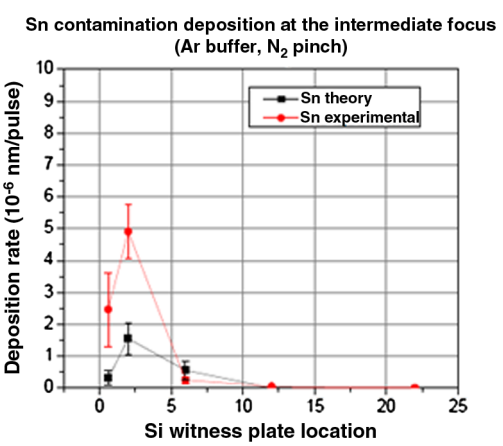

Fig. 11 Theoretical and experimental Sn deposition at the IF follow the same trends with pressure. At high pressures, transport is inhibited. Deposition is maximized at 2 mTorr; at this pressure, buffer gas scatters Sn away from the walls and toward the IF, while the mean–free-path is not sufficiently low to inhibit the transport of this Sn to the IF. The theoretical and experimental deposition magnitudes differ at low pressures. This is due to electrode sputtering and arcing, which produce low-energy Sn that is not accounted for in the energetic model. Pressures of 6 mTorr and above easily inhibit the transport of this low-energy Sn.

4.2 *Buffer Gas*

With the pinch gas fixed at 100 sccm of N_2 and the pressure fixed at 2 mTorr, the buffer gas was varied between He (4 AMU), Ne (20 AMU), and Ar (40 AMU). As shown in Fig. 12, the buffer gas mass plays an important role in debris transport. Figure 12(a) shows good agreement between experimental and theoretical flux measurements, while Fig. 12(b) provides insight into why the buffer gas mass is important.

Again, as with the pressure experiments, the experimental results are in good agreement with the model predictions. Figure 12(a) shows that, at 2 mTorr, the energetic buffer gas flux reaching the IF rises as buffer gas mass rises from 4 to 40 AMU. As shown in Fig. 12(b), this phenomenon is due to an increase in buffer gas energy at 20 and 40 AMU, as well as an increase in the number of species reaching the IF at 40 AMU. Energy transfer from the pinch gas to the buffer gas is affected both by the similarity between the masses of the pinch gas and buffer gas. The mass-similarity factor, γ, is given by Eq. (32), where m is the pinch gas mass and M is the buffer gas mass

$$\gamma = \frac{4mM}{(m+M)^2}. \tag{32}$$

Since the pinch atoms (Sn) have a mass of 118 AMU, γ is small for He buffer gas but larger for Ne and largest for Ar. Since the scattering cross-section is similar for Sn collisions with He and Ne, the change in γ is the main cause of the increase in energetic Ne flux compared to energetic He flux. The higher value of γ increases the energy transfer to Ar, as well; however, the cross-section is also much larger for Sn–Ar collisions. This increases the number of collisions and, therefore, the total amount of buffer gas scattered to the IF. Thus, since Ar is subject to both increased energy transfer and a larger number of collisions, the flux rises sharply when the buffer gas is changed from Ne to Ar.

Additionally, as shown in Fig. 13, Sn deposition at the IF experimentally rises when the buffer gas is Ar. The deposition results are in agreement with the model except for the large deposition rate caused by Ar buffer gas.

The reason for this error, as with the errors in Fig. 11, is electrode sputtering and arcing, which releases low-energy Sn atoms and particles that are not accounted for in the model. Ar, owing to its heavy mass, more easily sputters the Sn electrode.

The traditional reasoning behind using a heavy gas (such as Ar) as the buffer gas is the fact that such a gas will slow down and deflect Sn debris more effectively by colliding more frequently (due to the larger cross-section) and transferring more energy to the buffer gas (due to the higher mass). A system being used for EUV lithography will not have support brackets from dummy collector shells obscuring the line of sight from the pinch to the IF, so the ability to collide the high-energy Sn debris with the buffer gas atoms is important. This rationale is validated by noting that the model predicts (at 2 mTorr) that the fractional energy deposition in the buffer gas (as opposed to the walls, which, in a nonobscured system, could include the IF) is 43.5% for Ar, as opposed to 34.5% for Ne and 31.0% for He. However, as has been demonstrated theoretically and experimentally in this paper, it is not enough to simply deposit the pinch energy in the buffer gas, as this can aid the transport of low-energy Sn and high-energy buffer gas to the IF. As seen in Sec. 4.1, the pressure must be high enough to deter this transport.

4.3 *Pinch Gas*

Having gained an understanding of the transport of high-energy Sn atoms and the debris generated by collisions with Sn atoms, a brief exploration of energetic flux due to variations in the pinch feedstock gas was undertaken. Experimentally, the pinch gas was varied between He, Ne, and Ar at a constant pressure of 2 mTorr. The modeling was carried out using computational pinch gas atoms rather

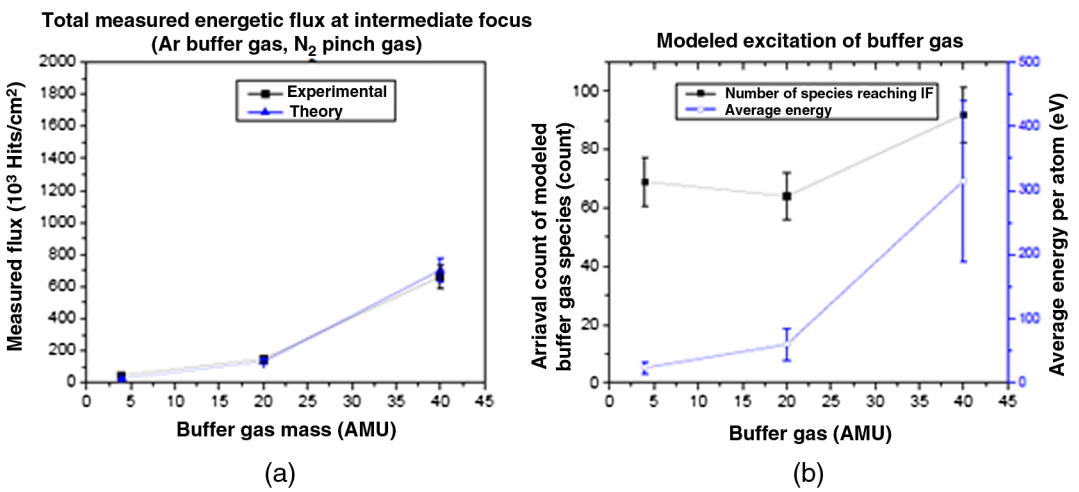

Fig. 12 (a) At 2 mTorr, the buffer gas mass is varied from 4 AMU (He) to 40 AMU (Ar), and the energetic flux reaching the IF increases. The model and experiments are in good agreement. (b) The model illuminates the reasons behind the high flux at 40 AMU. As buffer gas mass increases and becomes closer to the mass of Sn, energy transfer from Sn to the buffer gas increases, leading the average buffer gas energy to be greater for Ne than He and greater for Ar than Ne. Additionally, the Ar flux is also made large by an increase in the number of species reaching the IF. This occurs because of a large Sn–Ar interaction cross-section, which causes more Ar atoms to collide with Sn and become energized.

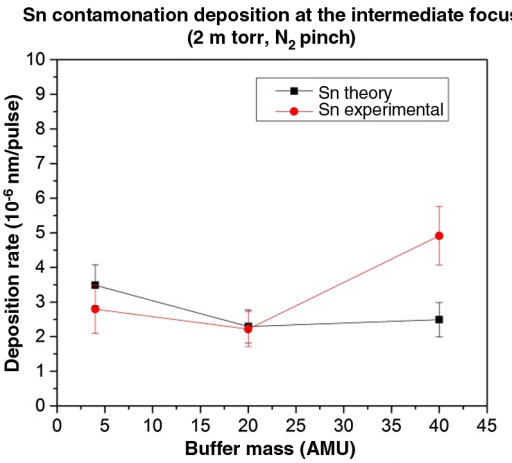

Fig. 13 With the pressure held constant at 2 mTorr, theoretical and experimental Sn deposition are in agreement for He and Ne buffer gas. However, the experimental Sn deposition is much larger than predicted by the model. As in Fig. 11, the deposition discrepancy is due to electrode sputtering and arcing, which are more common with Ar buffer gas. These results, as well as those in Fig. 12, show that a heavy buffer gas, while it can remove energy from Sn, can also cause energetic buffer gas fluxes and increased deposition at the IF. Pressure must be chosen carefully to reduce the transport of both Sn and energetic buffer gas without sacrificing too much EUV transmission.

than computational Sn atoms; the energies of these atoms were chosen according to ion energy distributions functions measured for each individual pinch gas, similar to the distribution function for N_2 in Fig. 2. It is important to note that modern commercial EUV sources use Sn alone without a feedstock gas, which renders feedstock gas variations unrealistic in relation to commercial sources. Additionally, the model calibration factor of 158, calculated in Sec. 3, was determined using modeled Sn atoms rather than modeled feedstock gas atoms; this will cause magnitude errors in simulations that used modeled feedstock atoms. However, despite this, the model and experiments ought to share the same underlying physics. Thus, variations of pinch gas were performed to track the physics of energy exchange and to further verify that the model captures the correct underlying physics.

Figure 14 confirms that, though the use of the Sn calibration factor causes error in the magnitude of hits, both theory and experiment show the same trends. Since the buffer gas was Ar, energy transfer was maximized with Ar pinch gas atoms. This, combined with the large Ar–Ar cross-section, caused a high flux at the IF for Ar pinch gas relative to the two other pinch gases.

5 Conclusions

This investigation was performed to achieve a better understanding of the mechanisms by which debris is transported to the IF of an EUV light source from the energetic plasma used to create 13.5 nm photons. It was demonstrated that the interactions between the pinch species and the buffer gas are the primary cause of the generation of debris and how it is distributed throughout the chamber. This has been shown both by a Monte Carlo model and by experiments on a Z-pinch plasma source. The model has the capability to predict debris transport to the IF in any EUV source with a quantifiable energetic output.

While it is desirable to choose a buffer gas in a way that maximizes the collision frequency and energy transfer with energetic Sn atoms in order to mitigate the effects of

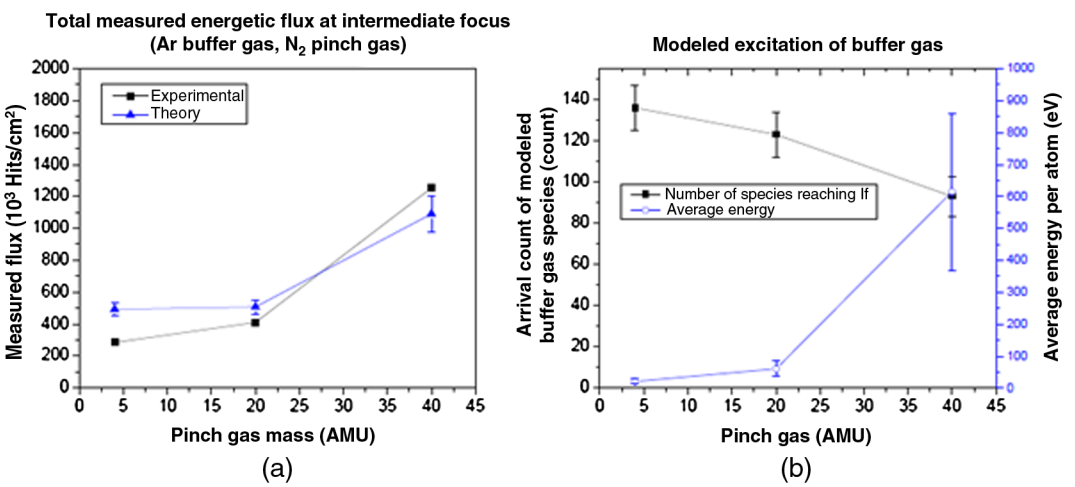

Fig. 14 (a) The pinch gas was varied between He, Ne, and Ar with Ar buffer gas at a pressure of 2 mTorr. Simulations were carried out with 10,000 atoms of each pinch gas, rather than Sn. Since the same calibration factor (158) was used in these simulations as for the Sn atom simulations, error is present between the model and experiments. Nevertheless, the underlying physics remains the same, and the model and experiments thus display the same trends. As pinch gas mass is increased, the energetic flux to the IF increases, especially when Ar is the pinch gas. (b) The reason for the flux increase with pinch gas mass is shown. As the pinch gas mass is increased, it approaches the mass of the Ar buffer gas, causing greater energy transfer in collisions. While this means that it takes fewer collisions to remove the energy from a pinch atom, the cross-section also grows as the pinch atoms get larger. Thus, the increased cross-section keeps the number of species reaching the IF from decaying as quickly as their energy increases. In particular, energy transfer is maximized for same-species collisions (Ar pinch gas with Ar buffer gas). This fact, combined with a large Ar–Ar cross-section, causes the energetic Ar flux to the IF to be high.

energetic Sn, this can also facilitate increased transport of low-energy Sn atoms and energetic buffer gas atoms to the IF if the pressure is not chosen carefully, leading to potential damage of downstream components in an EUV tool. While increasing the pressure enough can decrease debris transport, this will need to be balanced against the possibility of EUV absorption in a high-pressure environment. Currently, industrial strategy seems to the use of very high flows and pressures of H_2 buffer gas, due to the EUV transmission of H_2. However, even H_2 does absorb some EUV, making it imperative to use a pressure that is no higher than necessary. The model detailed in this paper can be used to help quantify debris transport and inform source developers as to how much buffer gas is necessary to prevent debris transport.

Acknowledgments

The authors would like to acknowledge the assistance of SEMATECH Inc. in funding and contributing to the development of SNIFFED. Furthermore, part of this research was carried out at the Frederick Seitz Materials Research Laboratory Central Facilities, University of Illinois, which was partly supported by the U.S. Department of Energy under Grant No. DEFG02-91-ER45439.

References

1. A. A. Schafgans et al., "Performance optimization of MOPA pre-pulse LPP light source," *Proc. SPIE* **9422**, 94220B (2015).
2. D. T. Attwood, *Soft X-Rays and Extreme Ultraviolet Radiation*, Cambridge University Press, Cambridge (1999).
3. H. Maury et al., "Non-destructive X-ray study of the interphases in Mo/Si and Mo/B4C/Si/B4C multilayers," *Thin Solid Films* **514**(1–2), 278–286 (2006).
4. C. Hecquet et al., "Design, conception, and metrology of EUV mirrors for aggressive environments," *Proc. SPIE* **6586**, 65860X (2007).
5. R. A. Burdt et al., "Laser wavelength effects on the charge state resolved ion energy distributions from laser-produced Sn plasma," *J. Appl. Phys.* **107**(4), 043303 (2010).
6. D. T. Elg et al., "Magnetic debris mitigation system for EUV sources," *J. Micro/Nanolithogr. MEMS MOEMS* **14**(1), 013506 (2015).
7. J. Sporre et al., "Ionic debris measurement of three extreme ultraviolet sources," *J. Appl. Phys.* **106**(4), 043304 (2009).
8. D. N. Ruzic et al., "Reduction of ion energies from a multicomponent Z-pinch plasma," *IEEE Trans. Plasma Sci.* **35**(3), 606–613 (2007).
9. D. Andruczyk et al., "Energetic ion and neutral energy analyzer for extreme-ultraviolet sources," *Proc. SPIE* **8322**, 832237 (2012).
10. Y. Teramoto et al., "Development of Sn-fueled high power DPP EUV source for enabling HVM," *Proc. SPIE* **6517**, 65173R (2007).
11. D. T. Elg et al., "Collector optic cleaning by in-situ hydrogen plasma," *Proc. SPIE* **9422**, 9422H (2015).
12. J. Sporre et al., "In-situ Sn contamination removal by hydrogen plasma," *Proc. SPIE* **8322**, 83222L (2012).
13. J. Sporre and D. N. Ruzic, "Debris transport analysis at the intermediate focus of an extreme ultraviolet light source," *J. Micro/Nanolithogr. MEMS MOEMS* **11**(2), 021117 (2012).
14. K. C. Thompson et al., "Experimental test chamber design for optics exposure testing and debris characterization of a xenon discharge produced plasma source for extreme ultraviolet lithography," *Microelectron. Eng.* **83**, 476–484 (2006).
15. E. L. Antonsen et al., "Ion debris characterization from a Z-pinch extreme ultraviolet light source," *J. Appl. Phys.* **99**, 063301 (2006).
16. J. R. Sporre, "Detection of energetic neutral flux emanating from extreme ultraviolet light lithography source," MS Thesis, Department of Nuclear, Plasma and Radiological Engineering, University of Illinois at Urbana-Champaign (2010).
17. J. Greenwood, "The correct and incorrect generation of a cosine distribution of scattered particles for Monte-Carlo modelling of vacuum systems," *Vacuum* **67**(2), 217–222 (2002).
18. J. F. Ziegler et al., *SRIM–the Stopping and Range of Ions in Matter*, Lulu Press Company, Morrisville, NC (2008).
19. D. N. Ruzic, "The effects of elastic scattering in neutral atom transport," *Phys. Fluids B* **5**(9), 3140–3147 (1993).
20. A. M. Myers et al., "Monte Carlo simulations of sputter atom transport in low-pressure sputtering: the effects of interaction potential, sputter distribution, and system geometry," *J. Appl. Phys.* **72**(7), 3064–3071 (1992).
21. A. A. Abrahamson, "Born-Mayer-type interatomic potential for neutral ground-state atoms with Z = 2 to Z = 105∗," *Phys. Rev.* **178**(1), 76–79 (1969).
22. S. W. Van Sciver, *Helium Cryogenics*, 2nd ed., Springer, New York (2012).
23. N. Mehdipour et al., "A perturbed hard-sphere equation of state for liquid metals," *Phys. Chem. Liq.* **49**(3), 347–354 (2011).
24. M. S. Child, *Molecular Collision Theory*, Academic Press, New York (1974).

John R. Sporre is a reactive ion etching process engineer at IBM developing methods for next-generation semiconductor manufacturing. His past areas of research have included energetic plasma ion and neutral characterization, laser-assisted plasma formation, as well as plasma-based surface manipulation. He earned his PhD from the University of Illinois at Urbana-Champaign in 2013.

Daniel T. Elg is a doctoral student at the Center for Plasma-Material Interactions at the University of Illinois at Urbana-Champaign. He received his BS degree in electrical and computer engineering from Olin College in 2011 and his MS degree in nuclear, plasma, and radiological engineering from the University of Illinois in 2013. He is a student member of SPIE. His research interests include plasma physics and plasma processing applications.

Kishor K. Kalathiparambil received his PhD in physics from Devi Ahilya University, Indore, India. Afterwards, he spent two years as a postdoctoral associate at the National Center for Scientific Research at Aix-Marseille University, France. He is currently in his third year of a postdoctoral research appointment at the Center for Plasma Materials Interactions at the University of Illinois at Urbana-Champaign, where he is working on developing liquid lithium-based plasma facing components for fusion devices.

David N. Ruzic is Abel Bliss Professor of Nuclear, Plasma and Radiological Engineering, and director of the Center for Plasma-Material Interactions at the University of Illinois at Urbana-Champaign. He is a fellow of the American Nuclear Society, the American Vacuum Society (AVS), and the Hertz Foundation. He also serves as the scientific director for the International Union of Vacuum Science, Techniques, and Applications.